

# Combining $C_n^2$ models to forecast the optical turbulence at Paranal

Omar Cuevas<sup>1,2,3★</sup>, J. C. Marín<sup>1,3,4★</sup>, J. Blázquez<sup>1,2,5</sup> and C. Meyer<sup>3</sup>

<sup>1</sup>*Instituto de Física y Astronomía, Universidad de Valparaíso, Valparaíso, 2340000, Chile*

<sup>2</sup>*Facultad de Ciencias Astronómicas y Geofísicas, Universidad Nacional de La Plata, La Plata, B1900FWA, Argentina*

<sup>3</sup>*Centro de Estudios Atmosféricos y Cambio Climático (CEACC), Universidad de Valparaíso, Valparaíso, 2340000, Chile*

<sup>4</sup>*Departamento de Meteorología, Universidad de Valparaíso, Valparaíso, 2340000, Chile*

<sup>5</sup>*Consejo Nacional de Investigaciones Científicas y Técnicas (CONICET), Buenos Aires, C1425FQB, Argentina*

Accepted 2024 February 16. Received 2024 January 23; in original form 2023 June 28

## ABSTRACT

We applied a combination of models to improve the forecasts of refractive index structure coefficient ( $C_n^2$ ) profiles and seeing at Paranal using high-temporal and spatial resolution simulations with the Weather Research and Forecasting model. We assessed our method with Stereo–SCIntillation Detection And Ranging observations from several nights between 2016 and 2018. The combined approach consists of the turbulent kinetic energy-based model to estimate the  $C_n^2$  profile within the boundary layer and another model for the free atmosphere. We tested the Dewan, Jackson–Dewan, and Gladstone models. The implementation of the combined method gives better results than those obtained using each model separately for the whole atmospheric column. However, a much better agreement with observations is obtained when we use a calibration method to improve the results. Calibrated seeing forecasts at Paranal showed a root mean squared error of 0.30 arcsec and a bias around  $-0.1$  arcsec for all the nights of 2017 and 2018, which are similar to previous results obtained at Paranal during the same nights. Due to its performance and rapid execution, the proposed methodology could be implemented as an operational tool to forecast the  $C_n^2$  profiles and the seeing at Paranal and potentially over other astronomical sites around the world.

**Key words:** turbulence – atmospheric effects – methods: numerical – site testing – software: simulations.

## 1 INTRODUCTION

Atmospheric turbulence is the main factor affecting the quality of images collected at ground-based astronomical observatories. The vertical profile of the refractive index structure coefficient ( $C_n^2$ ) is usually used to describe the turbulence intensity of the atmosphere. Another widely used parameter, the seeing, quantifies the blurring, and twinkling of astronomical objects caused by atmospheric turbulence. Several methods have been proposed to estimate the  $C_n^2$ , which have been based on *in situ* measurements taken by radiosondes (Coulman et al. 1988; Dewan et al. 1993; Jackson 2004; Trinquet & Vernin 2007; Basu 2015), and remote-sensing data (Coulman et al. 1988; Fiorino 2014).

The knowledge of the optical turbulence profile is crucial in the current operations of astronomical facilities, particularly for the new generations of large, very large, and extremely large telescope projects, where the negative impact of turbulence is amplified. For this reason, being able to predict several days in advance the evolution of the optical turbulence over the whole atmospheric column at astronomical observatories will largely benefit the schedule of their scientific activities, reducing, as a consequence, the operational costs.

A large increase in computer power, better observational networks and data assimilation systems, and enhanced knowledge of the physical mechanisms controlling atmospheric processes have caused

a notable improvement in numerical weather forecasts in the last decades (Bauer, Thorpe & Brunet 2015). Many studies have focused on implementing different methods to calculate the  $C_n^2$  vertical distribution from the outputs of global and regional numerical weather models to improve the atmospheric turbulence forecasts at specific astronomical observatories around the world.

Examples of studies using global atmospheric data are those of Ye (2011), who implemented the model proposed by Trinquet & Vernin (2007) to estimate the  $C_n^2$  profiles at different sites around the world using the Global Forecast System. In addition, Osborn & Sarazin (2018) applied the model described in Masciadri et al. (2017) to estimate the optical turbulence at Paranal using the ERA5 (ECMWF Reanalysis v5) global re-analysis data set from the European Centre for Medium-range Weather Forecasts. Despite the reasonably good results obtained in those studies, the spatial and temporal resolutions of global data sets represent a limitation, specifically in estimating the planetary boundary layer (PBL) turbulence over complex terrain since global circulation models include, in general, a coarse representation of the topography and the influence of local effects on turbulence are not well represented.

Among the advantages of implementing regional models to forecast the atmospheric conditions at astronomical sites is an improved representation of the local topography and the ability to provide forecasts of atmospheric variables at increased temporal and horizontal resolutions. Due to this, a large number of studies have implemented methods to estimate different parameters that characterize the optical turbulence over astronomical observatories using mesoscale models,

\* E-mail: [omar.cuevas@uv.cl](mailto:omar.cuevas@uv.cl) (OC); [julio.marin@meteo.uv.cl](mailto:julio.marin@meteo.uv.cl) (JCM)

aiming to provide its forecast over different astronomical sites (Masciadri & Jabouille 2001; Cherubini, Businger & Lyman 2008; Cherubini & Businger 2013; Giordano et al. 2013, 2014; Masciadri et al. 2017; Cuevas, Curé & Escárate 2018; Lyman, Cherubini & Businger 2020; Masciadri, Turchi & Fini 2023; Quatresooz et al. 2023; Shikhovtsev et al. 2023)

The PBL is the atmospheric layer closest to the Earth’s surface that directly feels its effects (e.g. friction, warming, cooling, etc.) and responds to them on time-scales of the order of a few hours or less (Stull 1988). As a result, the PBL and the free atmosphere (above the PBL) are characterized by very different circulation regimes and processes. Osborn et al. (2018), using Stereo–SCIDAR observations at Paranal, showed that 40 per cent of the turbulence is confined within the PBL to an altitude below 600 m, which indicates that the turbulence representation within the PBL is crucial to provide accurate forecasts of this parameter at this and other sites.

In this study, we aim to implement a methodology to forecast the  $C_n^2$  vertical profile and the seeing at Paranal, using a combination of two  $C_n^2$  formulations; one for the PBL and another one for the free atmosphere. We will calculate  $C_n^2$  and seeing forecasts using high temporal and spatial resolution regional numerical simulations from the Weather Research and Forecasting (WRF) model. In addition to this, we also aim to implement a calibration method to improve the estimation of the vertical structure of turbulence at the study site. Forecasts of turbulence parameters (calibrated and non-calibrated) will be assessed with S–SCIDAR observations from several campaigns conducted at Paranal between 2016 and 2018.

The remainder of this paper is organized as follows: The details of the WRF model configuration employed, the methods used to compute the  $C_n^2$  profiles, the calibration implemented, and the observations used to assess the simulations are described in Section 2. The results can be found in Section 3, and a discussion of results and the Conclusions are provided in Section 4.

## 2 DATA AND METHODS

### 2.1 Numerical weather prediction model

The Weather Research and Forecasting (WRF)<sup>1</sup> model is a mesoscale numerical weather prediction system that is used both for operational forecasting and atmospheric research. Several research centres, agencies, and universities have contributed to developing and implementing new physics schemes, data assimilation, and numerical algorithms into the model. In addition, detailed data bases for land use, topography, and soil type are provided for high-resolution forecasts. Version 3.8.1 of the model (Skamarock et al. 2008) was used in this study.

The WRF model was run fully compressible, non-hydrostatic, with four nested domains centred at Paranal site (Fig. 1). The simulations included 75 vertical levels with increased density (22 levels) in the 0–1 km layer. Results from the innermost domain (d04), at 1 km horizontal resolution, were used in the study. Fig. 1 also shows a zoom-in to domain 4, highlighting the complex topography surrounding the site, which is included within the model. The Final Analysis from the National Centers for Environmental Prediction Global Data Assimilation System at 0.25 degree horizontal resolution (National Centers for Environmental Prediction, National Weather Service, NOAA, U.S. Department of Commerce 2015) provided

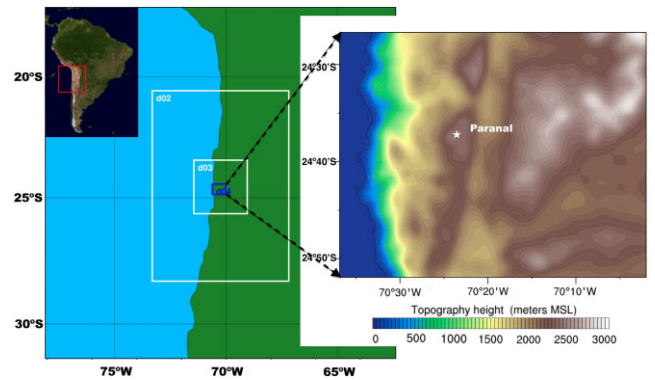


**Figure 1.** The WRF domain configuration employed in this study includes four nested domains at 27, 9, 3, and 1 km horizontal resolution. A zoom-in to the innermost domain (d04) with its complex terrain height (colour shading) and the location of the Paranal observatory are also shown.

initial and boundary conditions for the WRF simulations every six hours. The simulations started every day at 18 UTC and were run for 18 h. The first six hours of simulation on each day were not used to avoid initial model perturbations (e.g. spin-up errors). Therefore, the analysis of the nocturnal evolution of  $C_n^2$  profiles and seeing was performed from forecast hours 6 to 18. WRF outputs were saved every ten minutes, and the model was assessed with local observations.

The WRF model was configured using the Quasi-Normal Scale Elimination (QNSE; Sukoriansky, Galperin & Perov 2005) parametrization to solve the PBL processes. This is a 1.5-order local closure scheme that calculates the turbulent kinetic energy (TKE), which is used to estimate the  $C_n^2$ . A recent study where several PBL parameterizations were assessed with observations in the north of Chile showed a better agreement between the QNSE scheme and observations (Salfate et al. 2020). Longwave and shortwave radiation processes were calculated with the Rapid Radiative Transfer Model scheme (RRTMG; Iacono et al. 2008). We used the Noah Multi-Physics land surface model (Noah-MP; Niu et al. 2011) and the WRF Single-Moment 5-class microphysics (Hong, Dudhia & Chen 2004) in all domains. Finally, convection was not parametrized in domain 4, whereas the Grell-3D cumulus parametrization (Grell & Dévényi 2002) was used in domains 1–3.

### 2.2 Models to estimate the $C_n^2$ profiles

Several models to calculate the  $C_n^2$  profile as a function of atmospheric variables can be found in the literature. Most of them are based on the Tatarski relation (Tatarski’i 1961):

$$C_n^2 = \alpha M^2 L_0^{4/3} \quad (1)$$

where the  $C_n^2$  is related to the vertical gradient of the potential refractive index ( $M$ ) and the outer scale ( $L_0$ ), being  $\alpha$  a constant.

This section will describe the models used in this study to test our combined methodology to calculate the  $C_n^2$  profile.

#### 2.2.1 Dewan model

The Air Force Geophysics Laboratory proposed a model to calculate the  $C_n^2$  profile based on a large campaign of radiosondes launched in the United States (Dewan et al. 1993). This empirical model (called

<sup>1</sup><https://www.mmm.ucar.edu/wrf-model-general>

De afterwards) calculates the  $C_n^2$  profile using the following equation:

$$C_n^2 = \alpha \left( \frac{(79 \times 10^{-6} P)}{T^2} \right)^2 (0.1)^{4/3} \left( \frac{\partial T}{\partial Z} + \gamma_d \right)^2 10^{Y^*} \quad (2)$$

where  $\alpha = 2.8$ ,  $P$  is the pressure (hPa),  $T$  is the temperature (Kelvin),  $\gamma_d$  is the dry adiabatic lapse rate ( $\text{Km}^{-1}$ ), and  $Z$  is the height ( $m$ ). The parameter  $Y^*$  uses different expressions for the troposphere and the stratosphere:

$$\begin{aligned} Y^*(\text{Troposphere}) &= 1.57 + 40S, \\ Y^*(\text{Stratosphere}) &= 0.503 + 51.2S, \end{aligned} \quad (3)$$

where  $S$  is the vertical wind shear calculated by:

$$S = \left[ \left( \frac{\partial u}{\partial z} \right)^2 + \left( \frac{\partial v}{\partial z} \right)^2 \right]^{\frac{1}{2}} \quad (4)$$

and  $u$  and  $v$  are the  $x$ - and  $y$ - (zonal and meridional) wind components, respectively.

### 2.2.2 Modified Dewan model

Jackson (2004) proposed an improvement to the Dewan model (called JD afterwards), dividing the atmosphere into three layers: that below 5500 m (lower troposphere), from 5500 m to the tropopause (middle troposphere) and the stratosphere. In each of these three layers,  $Y^*$  is calculated using the following expressions:

$$\begin{aligned} Y_{LT} &= 2.9767 + 27.9804 \frac{dV}{dz} + 2.9012 \frac{dT}{dz} + 1.1843 \left( \frac{dT}{dz} \right)^2 \\ &\quad + 0.1741 \left( \frac{dT}{dz} \right)^3 + 0.0086 \left( \frac{dT}{dz} \right)^4, \end{aligned} \quad (5)$$

$$\begin{aligned} Y_{Tr} &= 0.7152 + 30.6024 \frac{dV}{dz} + 0.0003 \frac{dT}{dz} - 0.0057 \left( \frac{dT}{dz} \right)^2 \\ &\quad - 0.0016 \left( \frac{dT}{dz} \right)^3 + 0.0001 \left( \frac{dT}{dz} \right)^4, \end{aligned} \quad (6)$$

$$\begin{aligned} Y_{St} &= 0.6763 + 8.1569 \frac{dV}{dz} - 0.0536 \frac{dT}{dz} + 0.0084 \left( \frac{dT}{dz} \right)^2 \\ &\quad - 0.0007 \left( \frac{dT}{dz} \right)^3 + 0.00002 \left( \frac{dT}{dz} \right)^4, \end{aligned} \quad (7)$$

where  $\frac{dV}{dz}$  and  $\frac{dT}{dz}$  are the vertical wind shear and the vertical temperature gradient, respectively. Reference values for the tropopause height were obtained from a radiosondes campaign conducted at Paranal in 2009 (Chacón et al. 2010).

It is important to note that De and JD methods do not include the PBL in their formulations. However, we tested how these models represent the  $C_n^2$  profile within the PBL extending equations (3) and (5) down to the surface. In addition, the De and JD models are derived from radiosonde campaigns in the USA, where the geographical and atmospheric conditions may be different from those at Paranal. Therefore, besides implementing the JD model to calculate the  $C_n^2$  profile using the three equations (5)–(7), we also evaluated whether using only equation (6) for the whole atmospheric column gives better results at Paranal than using the original JD formulation with three layers.

### 2.2.3 Gladstone model

The Gladstone equation estimates the  $C_n^2$  profile based on the temperature structure constant ( $C_T^2$ ). Masciadri et al. (2017) proposed

a modification to this method replacing  $T^2$  by  $T\theta$  (called  $G_m$  afterwards), using the following expression:

$$C_n^2 = \left( \frac{80 \times 10^{-6} P}{T\theta} \right)^2 C_T^2, \quad (8)$$

where  $\theta$  is the potential temperature (Kelvin) and the temperature structure coefficient ( $C_T^2$ ) along the vertical path  $L$  is defined as:

$$C_T^2 = L^{\frac{4}{3}} \left( \frac{\partial \theta}{\partial z} \right)^2 \phi. \quad (9)$$

The  $\phi$  parameter represents the thermal and dynamic stability of the atmosphere (Masciadri & Jabouille 2001) and  $L$  can be expressed as a function of  $\theta$  and the TKE using:

$$L = \sqrt{\frac{2\text{TKE}}{\frac{g\partial\theta}{\theta\partial z}}}, \quad (10)$$

where  $g$  is the acceleration due to gravity. Similar to Osborn & Sarazin (2018), the TKE above the PBL was calculated as  $\text{TKE} = S^2$ , using equation (4) for  $S$ . Replacing equation (10) in (9), the final expression for  $C_n^2$  is:

$$C_n^2 = \phi \left( \frac{80 \times 10^{-6} P}{T\theta} \right)^2 L^{\frac{4}{3}} \left( \frac{\partial \theta}{\partial z} \right)^2. \quad (11)$$

Similar to that described in chapter 9 of Businger & Cherrubini (2011), and in Cuevas, Curé & Escárate (2018), we used  $\phi(z)$  as a function of altitude to calibrate the  $C_n^2$  for this specific astronomical site (Paranal). Other studies (Osborn & Sarazin 2018) have employed constant values for  $\phi$  to obtain a  $C_n^2$  expression that can be used on any site on the Earth.

### 2.2.4 Masciadri model for the PBL

Masciadri & Jabouille (2001) proposed a method to calculate the  $C_n^2$  from regional numerical simulations conducted with the Mesoscale No-Hydrostatic model (Meso-NH). This method is derived from Gladstone's relation and directly calculates the TKE and other atmospheric parameters using the following expression:

$$C_n^2 = 3.35 \times 10^{-6} P^2 \left( 1 - \frac{2R}{c_p} \right) \theta^{-\frac{10}{3}} \left( \frac{\partial \theta}{\partial z} \right)^{\frac{4}{3}} \text{TKE}^{\frac{2}{3}}, \quad (12)$$

In their model, the TKE is explicitly solved by the PBL parametrization in the regional weather model, which should be a more accurate approach than the simple expression employed in the  $G_m$  model, which is just a function of the wind shear ( $\text{TKE} = S^2$ ).

### 2.2.5 Mixed approach to calculate the $C_n^2$

Cuevas, Curé & Escárate (2018) found that combining a method to calculate the  $C_n^2$  profile within the PBL with another one to calculate the  $C_n^2$  above, gives better results than using each formulation separately for the whole atmospheric column. In this study, we implement this new methodology using equation (12) to calculate the  $C_n^2$  within the PBL, combined with another method to calculate the  $C_n^2$  above it, such as De, JD, or  $G_m$ .

The method used to calculate the  $C_n^2$  profile within the PBL depends on TKE. The TKE is explicitly calculated by the PBL parametrization (QNSE) in the WRF model. Above the PBL, the QNSE scheme provides TKE values that decrease with height to  $0.05 \text{ m}^2 \text{ s}^{-2}$ , similar to other PBL parametrizations (Mellor–Yamada–Janjic and Boulac) where the TKE decreases above the PBL

**Table 1.** Description of  $C_n^2$  models employed in this study.

Model name	Description	Equations
De	Dewan	2–4
DeM	Dewan + Masciadri	2–4, 12
DeM <sub>C</sub>	Dewan + Masciadri + Calibration	2–4, 12, 15
JD	Jackson–Dewan	2, 5–7
JD2	one-layer Jackson–Dewan	2, 6
JD2M	one-layer Jackson–Dewan + Masciadri	2, 6, 12
JD2M <sub>C</sub>	one-layer Jackson–Dewan + Masciadri + Calibration	2, 6, 12, 15
G <sub>m</sub>	Gladstone modified	11
G <sub>m</sub> M	Gladstone modified + Masciadri	11, 12
G <sub>m</sub> M <sub>C</sub>	Gladstone modified + Masciadri + Calibration	11, 12, 15

to a critical value of  $0.1 \text{ m}^2 \text{ s}^{-2}$  (Xie et al. 2012). Our mixed models, combining De, JD, and G<sub>m</sub> methods with equation (12) will be called DeM, JDM, and G<sub>m</sub>M, respectively, afterwards. A description of the models used in this study and their acronyms is shown in Table 1.

### 2.3 Seeing estimation

The astronomical seeing is estimated by calculating the Fried number,  $r_0$ , which vertically integrates the  $C_n^2$  using the expression found in Roddier (1981) and Vernin & Munoz-Tunon (1992):

$$r_0 = \left[ 0.423 \left( \frac{2\pi}{\lambda} \right)^2 \int_0^L C_n^2(z) dz \right]^{-\frac{3}{5}}, \quad (13)$$

where  $\lambda$  is the wavelength at which the telescope is observing, and similar to other authors (Masciadri, Vernin & Bougeault 1999; Cherubini, Businger & Lyman 2008), we used a standard value of  $\lambda = 0.5 \times 10^{-6} \text{ m}$ . Finally, the seeing ( $\epsilon$ ) is obtained using the relation:

$$\epsilon = 0.98 \frac{\lambda}{r_0} \quad (14)$$

### 2.4 Calibration technique for $C_n^2$

Due to systematic errors in model simulations, Masciadri & Jabouille (2001) proposed a calibration technique to improve the estimation of the  $C_n^2$  profile. In this study, we employed a similar methodology to calibrate the  $C_n^2$  from model results. The calibration was performed using the observed and simulated  $C_n^2$  to minimize the systematic errors obtained at different heights, implementing the following expression:

$$a_m(k) = \frac{\langle C_n^2(k)_{\text{obs}} \rangle_{\sum_{t=1}^T} C_n^2(t, k)_{\text{sim}}}{\sum_{t=1}^T C_n^2(t, k)_{\text{sim}}^2}, \quad (15)$$

where  $k$  indicates the  $k_{\text{th}}$  layer of the instrument and  $t$  varies from 1 to the total number of times (nt) where simulated turbulence profiles are available each night. The  $C_n^2(k)_{\text{obs}}$  and  $C_n^2(k)_{\text{sim}}$  are the observed and simulated profiles, respectively, and brackets indicate a nighttime average.

The  $a_m(k)$  parameter was applied to  $C_n^2$  profiles obtained from mixed models DeM, JD2M, and G<sub>m</sub>M. The calibrated  $C_n^2$  profiles from implemented mixed models will be called DeM<sub>C</sub>, JD2M<sub>C</sub>, and G<sub>m</sub>M<sub>C</sub>, afterwards, as described in Table 1. The  $a_m(k)$  profile was obtained considering only the 16 nighttime observations and simulations of 2016. It was finally applied to the  $C_n^2$  profiles obtained from the mixed models for all nights of 2017 and 2018. Note that with these criteria, we evaluated the forecasts' performance without including information used during the calibration process.

**Table 2.** Description of the S–SCIDAR data available during several campaigns conducted at Paranal between 2016 and 2018.

Year	Month	Night	Total by year
2016	April	26–29	–
	July	22–26	–
	Oct.	30–31	–
	Nov.	01–02	–
	Dec.	10–12	16
2017	March	07–09	–
	April	12–18	–
	May	05–09	–
	June	08–10	–
	July	03–09	–
	Aug.	03–08	–
	Nov.	04–09; 18–20; 29–30	–
	Dec.	01–02; 05–06; 08–16; 18	55
2018	Jan.	13–15; 18–24	–
	March	06–08	–
	April	26–29	–
	May	24–28	–
	June	23–28	–
	July	01–05; 24–27	36
	Totals	–	107

### 2.5 Observations

The observed  $C_n^2$  profiles at Paranal (2635 m.a.s.l) were obtained from the S–SCIDAR instrument (Vernin & Azouit 1983; Shepherd et al. 2013; Osborn et al. 2018) for 107 nights between 2016 April and 2018 July (Table 2) during several observational campaigns. This instrument has high precision, sensitivity, and resolution, providing information irregularly spaced in time every 2–5 min on 100 vertical levels separated every 250 m. The observed seeing was also obtained from the S–SCIDAR instrument, which also registered the wind speed and direction on each of the 100 layers. The estimated wind speed and direction were used to assess the model simulations, whose comparison is presented in Section 3.1.

## 3 RESULTS

### 3.1 Assessment of the WRF simulation

Osborn et al. (2016) described a methodology to estimate the wind speed and direction from turbulence measurements taken by the S–SCIDAR at the same specific heights the  $C_n^2$  values are obtained. In that study, the estimated wind speeds and directions were assessed with radiosondes and forecasts from a global circulation model (GCM), showing a good agreement with them regarding its correlation, BIAS, and root mean squared error (RMSE). Based on that, and since variations in wind speed and direction largely influence the turbulence at the site of interest, we will first assess the WRF simulated wind speed and direction with S–SCIDAR observations during the observing nights of 2016–2018. To this aim, the simulated wind profiles were interpolated to the same S–SCIDAR observing heights. We will focus on evaluating the model performance within and above the PBL.

The WRF simulated median wind speed profile shows a relatively good agreement with the observed median wind speed profile from the S–SCIDAR below 6000 m (Fig. 2a). The model shows a large Pearson linear correlation of 0.72 and an RMSE of  $3.6 \text{ m s}^{-1}$  below 500 m, whereas a slightly larger correlation (0.79) and a lower RMSE

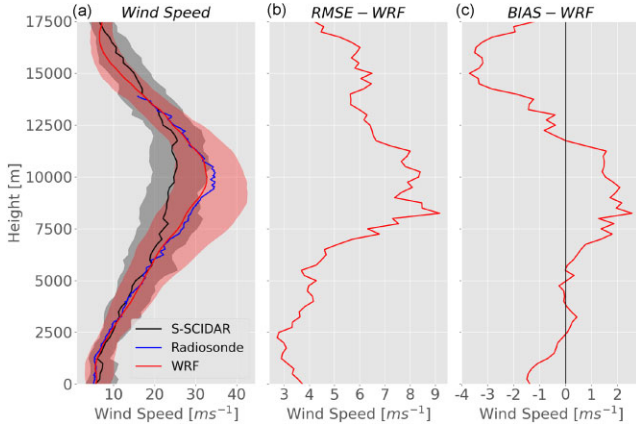


**Figure 2.** (a) The observed median (black) and WRF simulated (red) median wind speed profile, for all campaign days between 2016 and 2018, every 10 min. The blue line represents the median wind speed profile from the radiosondes launched at Antofagasta station at 12 UTC on each observing day. The coloured areas represent the interquartile range from observations and the WRF simulation, respectively. (b) and (c) show the RMSE and mean BIAS, respectively, between the simulation and observations.

of  $3.16 \text{ m s}^{-1}$  is indicated in the 500–1250 m layer (Fig. 2b). In addition, the simulated wind speed interquartile range is similar to that observed below 6000 m (Fig. 2a). The model mainly underestimates observations below 2500 m and above 12 000 m (Fig. 2c). On the other hand, the simulation overestimates the observed winds in the layer 6000–12 000 m height, showing its lowest performance in that layer with an RMSE  $> 6.0 \text{ m s}^{-1}$  (Fig. 2b). Superimposed in Fig. 2(a) is the median wind speed profile from the Antofagasta radiosonde, launched at 12 UTC, on every observing night of 2016–2018, at approximately 155 km to the north of Paranal. The observed median wind speed from the radiosonde is in close agreement with that from the WRF simulation over the whole atmospheric column showing the largest difference with the S-SCIDAR in the 6000–12 000 m, as previously mentioned.

Overall, the model represents reasonably well the wind speeds within the boundary layer and until 6000 m, where most of the turbulence occurs but its performance decreases above that height. Table 3 summarizes the statistics for the PBL and the free atmosphere, taking into account the layers 0–500, 500–1250, and 1250–17 500 m. It is important to mention that Osborn et al. (2016) showed that the estimated wind speed from the S-SCIDAR largely decreases its performance when compared with radiosondes for larger wind speed values (their Fig. 11), which generally occurs at higher heights. This adds some uncertainty to the assessment of wind speed forecasts at higher altitudes, partially accounting for the larger errors obtained for the WRF simulated wind speeds above the PBL.

**Table 3.** The RMSE, BIAS, and Pearson correlation coefficient ( $r$ ) between the simulated and the observed wind speed (WS) and wind direction (WD) over the 0–500, 500–1250, and 1250–17 500 m layers, and the whole column (0–17 500 m). The mean absolute error (MAE) is also displayed, but just for the wind direction.

Layer (m)	RMSE WS	BIAS WS	$r$ (WS)	RMSE WD (Degrees)	MAE WD (Degrees)	BIAS (Degrees)	$r$ (WD)
0–500	3.6	−1.4	0.72	116.4	76.2	−10	0.33
500–1250	3.16	−1.0	0.79	75.5	46.8	27.9	0.4
1250–17 500	5.6	−0.2	0.85	42.6	22.1	−49.6	0.5
All	5.3	−0.4	0.87	57	30	−40	0.53

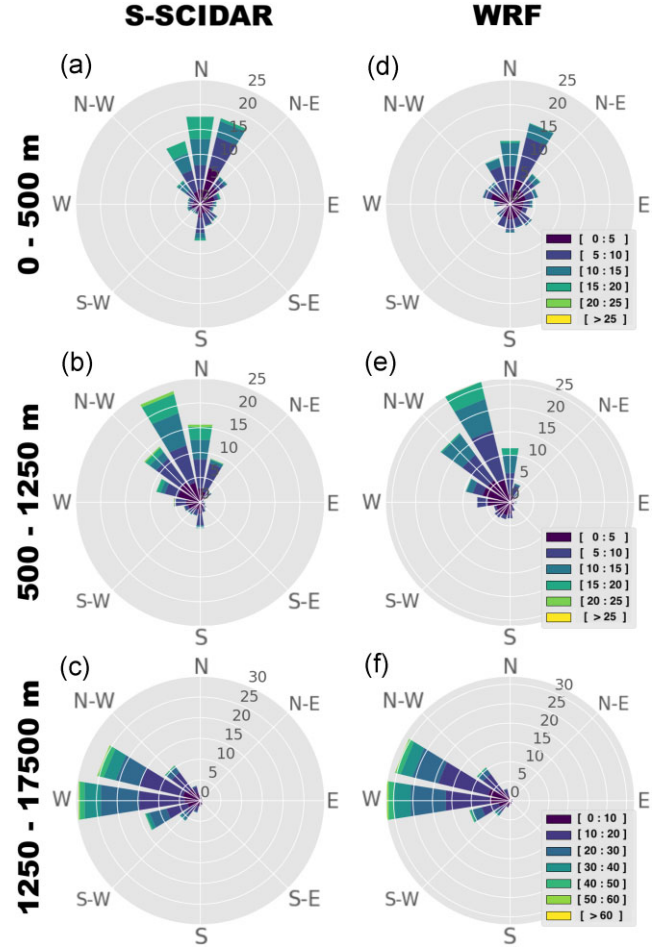


**Figure 3.** Wind rose plots derived from wind speed and direction from the S-SCIDAR for the (a) 0–500 m, (b) 500–1250 m, and (c) 1250–17 500 m layers, for all the S-SCIDAR heights and all campaign days between 2016 and 2018, every 10 min. (d)–(f) are the same as (a)–(c), but for the WRF model. The circles represent the data frequency in per cent and the colours indicate the wind speed ranges.

The observed wind predominantly flows between the north–north-west and the north–north-east in the closest layer to the ground (Fig. 3a) whereas it predominantly comes from the north–north-west in the 500–1250 m layer (Fig. 3b). Above the PBL (1250–17 500 m), the wind blows predominantly from the west and west–north-west (Fig. 3c). The model shows the lowest performance near the surface, showing a much lesser fraction of times the wind coming from the north–north-west and the north in the 0–500 m layer, as was observed (Fig. 3a,d). As a result, the comparison with observations shows a Pearson correlation coefficient of 0.3 and a mean absolute error

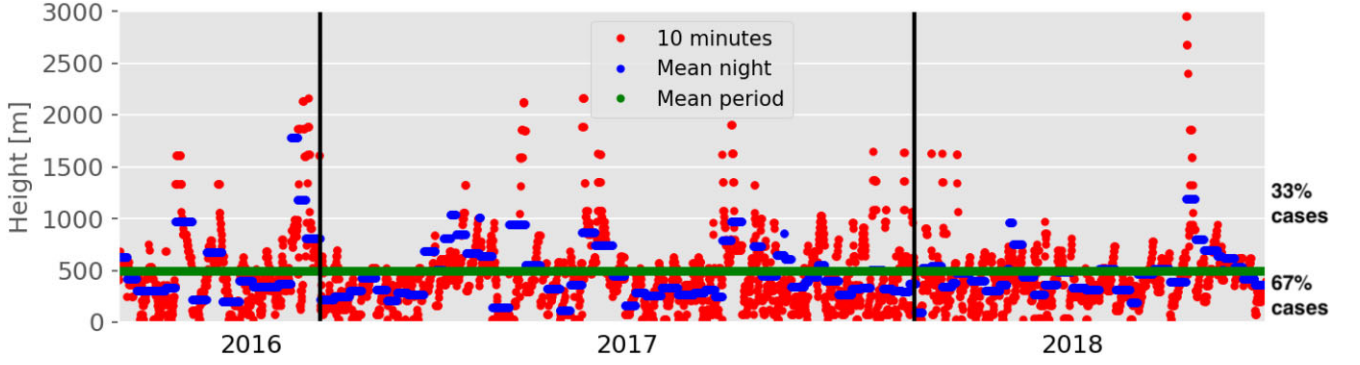


**Figure 4.** Temporal evolution of simulated PBL heights from WRF every 10 min (red dots) and PBL heights averaged over each observing night (blue dots). The mean PBLH averaged over all observing nights (green horizontal line) described in Table 2 is also displayed. The vertical black lines represent the times of the last observations in 2016 and 2017, respectively. The 10-min and nocturnal mean PBLH are just displayed as a continuous time series, without considering the periods with no data between observing nights.

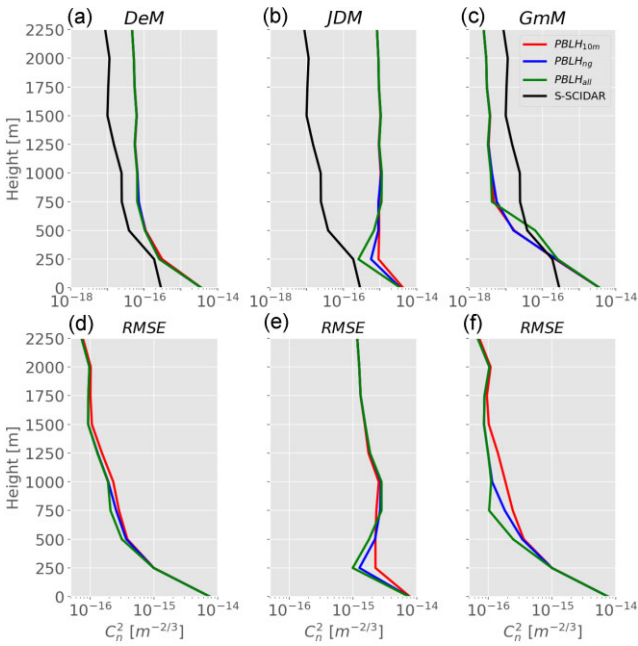


**Figure 5.** The observed  $C_n^2$  median profile from the S-SCIDAR (black line), and the simulated  $C_n^2$  median profiles calculated with the DeM, JDM, and GmM models using the PBLH obtained from WRF outputs every 10 min (red), the mean PBLH averaged over each observing night (blue), and the mean PBLH averaged over all observing nights (green) between 2016 and 2018.

**Table 4.** RMSE and BIAS between the simulated and the observed  $C_n^2$  profiles for the mixed models DeM, JDM, and GmM using three different PBLH estimations: PBLH<sub>10m</sub>, PBLH<sub>ng</sub>, and PBLH<sub>all</sub>.

Model	RMSE ( $m^{-2/3}$ ) $\times 10^{-15}$	BIAS ( $m^{-2/3}$ ) $\times 10^{-16}$
DeM-PBLH <sub>10m</sub>	2.46	6.20
DeM-PBLH <sub>ng</sub>	2.46	6.10
DeM-PBLH <sub>all</sub>	2.46	6.06
JDM-PBLH <sub>10m</sub>	3.08	16.80
JDM-PBLH <sub>ng</sub>	3.01	15.88
JDM-PBLH <sub>all</sub>	2.99	15.60
GmM-PBLH <sub>10m</sub>	2.46	5.52
GmM-PBLH <sub>ng</sub>	2.45	5.48
GmM-PBLH <sub>all</sub>	2.45	5.46

(MAE) of 76 degrees (Table 3). The wind direction is better simulated above 500 m. The absolute errors decrease and the correlation increases, in general, above the first layer, showing a correlation coefficient of 0.4 and an MAE of 47 degrees in the 500–1250 m layer, and a correlation coefficient of 0.5 and an MAE of 22 degrees in the free atmosphere (Table 3).

In summary, the performance of the simulated wind speed decreases whereas that of the wind direction increases with height at Paranál. Despite that, the statistics closest to the ground are within the range of errors found in other studies around the world over complex topography (Jiménez & Dudhia 2013; Gómez-Navarro, Raible & Dierer 2015). Thus, the above-mentioned discussion indicates that the WRF simulation can be used with confidence to estimate the  $C_n^2$  profiles and seeing over the study site, whose results will be presented in the following sections.

### 3.2 PBL height

Before showing how the mixed model improves the estimated turbulence profiles from the WRF simulation, we will include a short discussion on how we selected the PBL height (PBLH). The mixed methodology implemented in this study uses a model to estimate the  $C_n^2$  within the PBL and another model to calculate it above it. Thus, an accurate estimation of the PBLH is necessary. We use the PBLH calculated by the PBL parametrization in the WRF model supported by the fact that the model has shown a reasonably good agreement representing the observed PBLH over complex terrains of different characteristics in several studies (Banks et al. 2016; Roşu et al. 2019; Yang et al. 2022).

Fig. 4 shows the time evolution of the nighttime simulated PBLH obtained every 10 min (PBLH<sub>10m</sub>, red dots), the simulated mean PBLH averaged over each night (PBLH<sub>ng</sub>, blue dots), and the simulated mean PBLH calculated over all available nights (PBLH<sub>all</sub>, solid green line). The PBLH<sub>10m</sub> largely varies over the year and even during an observing night, from several meters to nearly 3000 m above the ground. Based on that, we conducted a sensitivity test comparing the observed median  $C_n^2$  profile, averaged over all the observing nights, with the median of simulated  $C_n^2$  profiles using the three different PBLH estimations (PBLH<sub>10m</sub>, PBLH<sub>ng</sub>, and PBLH<sub>all</sub>) to assess whether our results would be notably influenced by the way we select the PBLH in this study. The three different median  $C_n^2$  profiles from the mixed model DeM (Fig. 5a) are close to each other, showing the same RMSE and similar BIAS when compared

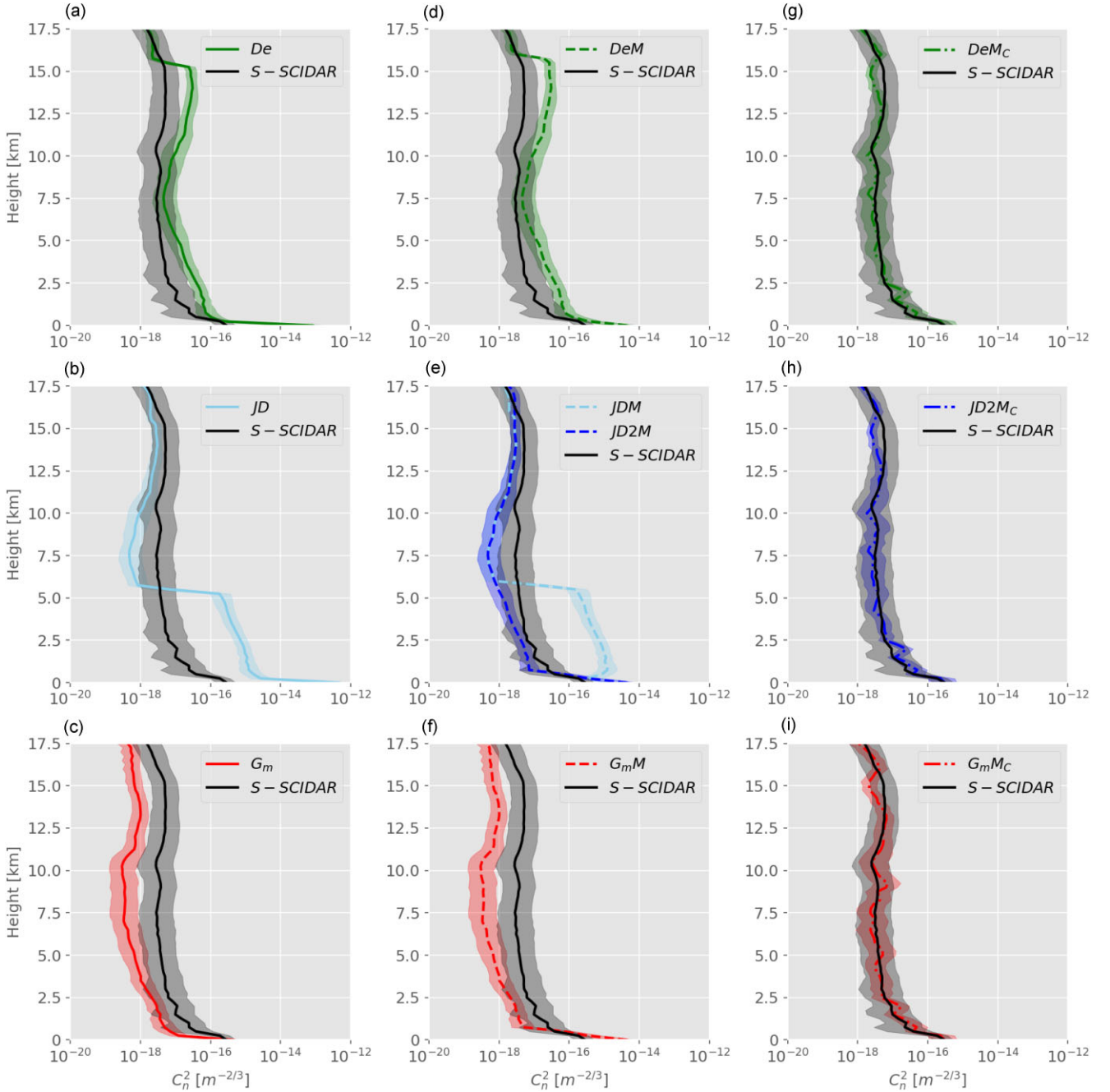


**Figure 6.** Median  $C_n^2$  profiles from the S–SCIDAR (black) and simulated from raw (a) De, (b) JD, (c)  $G_m$ , and mixed (d) DeM, (e) JD and one-layer JD2M, and (f)  $G_mM$  models for all observing nights between 2016 and 2018. (g)–(i) are the same as (d)–(f), but for the mixed calibrated models DeM<sub>C</sub>, JD2M<sub>C</sub>, and  $G_mM_C$ , respectively, for the observing nights of 2017 and 2018. See the legends for details. The colour areas show the observed and simulated interquartile range, respectively.

to observations (Fig. 5d and Table 4). Since the PBLH selection only affects the  $C_n^2$  calculation within the PBL and the PBLH<sub>10m</sub> is almost always below 2000 m (Fig. 4), the y-axis limits in Fig. 5 ranges between the surface and 2250 m. The simulated median  $C_n^2$  profiles from mixed models JD2M and  $G_mM$  using the three PBLH estimations show slight differences among them (Fig 5b,c), with the  $C_n^2$  profile obtained using the PBLH<sub>all</sub> showing the smallest RMSE and BIAS (Fig 5e,f and Table 4). Overall, since the  $C_n^2$  profile calculated with the three mixed models using the mean PBLH (PBLH<sub>all</sub>) shows a better agreement with observations, we used the

PBLH<sub>all</sub> when we calculated the  $C_n^2$  from mixed models in this study. The next section will show how the mixed models improve the estimation of turbulence using the Dewan, Jackson–Dewan, and Gladstone modified models.

### 3.3 $C_n^2$ profiles

As previously mentioned, we used the methods of Dewan (De), Jackson–Dewan (JD), and Gladstone modified ( $G_m$ ) to estimate the  $C_n^2$  profiles during all observing nights described in Table 2. The

simulated  $C_n^2$  profiles from each model were interpolated to the same heights of the S–SCIDAR instrument, distributed every 250 m from the ground to 17.5 km height. Thus, all the  $C_n^2$  profiles will be presented starting at the altitude of Paranal (2635 m.a.s.l.). In addition, the observed  $C_n^2$  profiles were interpolated every 10 min to the same temporal resolution of model outputs.

The simulated median  $C_n^2$  profile from the De model, calculated with all the available observing nights, is very close to the observed profile above 15 km but overestimates observations below it (Fig. 6a). The largest errors are shown close to the surface, which should be expected since we extended the  $C_n^2$  calculation down to the surface, and the De formulation does not include the PBL. The simulated median  $C_n^2$  profile from the JD model changes abruptly around 5.5 km, underestimating the observed profile above that height and overestimating it underneath (Fig. 6b). This is likely a result of the three-layer formulation in this method [equations (5), (6), and (7)] since the expression to calculate the  $C_n^2$  profile changes at 5.5 km. The largest errors with this model are shown below 5.5 km, particularly at the levels close to the surface. This is also a result of extending the calculation of the  $C_n^2$  profile down to the surface, as previously mentioned. The simulated  $C_n^2$  profile from the  $G_m$  model underestimates the observations in the whole atmospheric column, but it shows a closer agreement near the surface compared with the other models (Fig. 6c). This method does include the PBL in its formulation, contrary to De and JD models. Regarding the variability of the  $C_n^2$  profile during each observing night, the simulated  $C_n^2$  profiles from the three models (De, JD, and  $G_m$ ) are less variable than that observed. Overall, among the three models,  $G_m$  shows, in general, the best agreement with observations regarding its median value, daily variability, and vertical structure.

When we implemented the mixed models (DeM, JDM, and  $G_m$ M), combining De, JD, and  $G_m$  models above the PBL with Masciadri’s model within the PBL, the simulated  $C_n^2$  profile is improved within the PBL, except at the surface in the  $G_m$ M model (Fig. 6d–f). As mentioned in Section 2.2.2, we also calculated the  $C_n^2$  profile with the JD model but only using equation (6) for the whole atmospheric column to test whether it shows a better agreement with observations than the original three-layer formulation. The new model is named JD2M afterward. The  $C_n^2$  profile from the JD2M model mainly underestimates the observations (except at the surface) but largely reduces the  $C_n^2$  overestimation between the surface and 5.5 km (Fig. 6), showing a median profile closer to that observed. These results highlight the fact that, at least at Paranal, it would be better to use the JD2M than the JD method. From now on, we will use the JD2M instead of the JDM model in our analysis.

A closer look at the  $C_n^2$  profiles in the first 1000 m above the ground (Fig. 7) better indicates that the implementation of the mixed models improves the  $C_n^2$  representation within the PBL (colour dashed lines in the figure), particularly below 750 m, where turbulence is stronger. However, significant differences with observations still exist above the PBL and at specific heights within it. To improve even more the representation of turbulence profiles in our simulations, we applied the calibration method described in Section 2.4 to all the mixed models.

The calibrated  $C_n^2$  profiles (DeM<sub>C</sub>, JD2M<sub>C</sub>, and  $G_m$ M<sub>C</sub>) calculated from mixed models during the observing nights of 2017 and 2018 largely improve the  $C_n^2$  representation in all models over the free atmosphere (Fig. 6 g–i), and even within the PBL (Fig. 7). This is indicated by a median value in the calibrated-mixed models (DeM<sub>C</sub>, JD2M<sub>C</sub>, and  $G_m$ M<sub>C</sub>) that is much closer to observations than the median profiles from mixed models without calibration (DeM, JD2M, and  $G_m$ M). However, the variability of calibrated  $C_n^2$  profiles

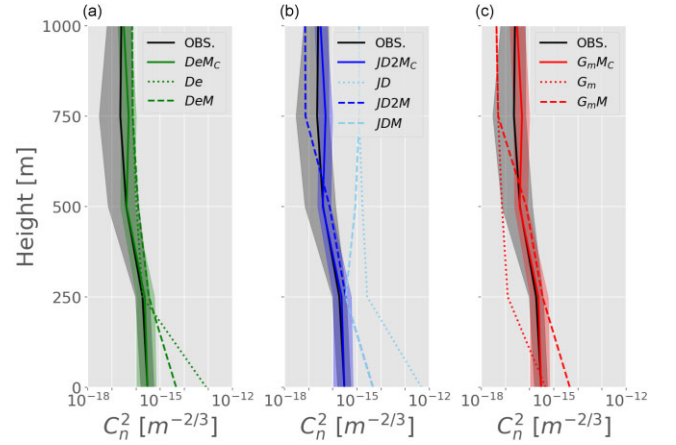


**Figure 7.** Zoom-in to Fig. 6 showing the observed median  $C_n^2$  profiles and simulated median profiles from (a) Dewan, (b) Jackson–Dewan, and (c) Gladstone raw, mixed, and mixed-calibrated models within the PBL (0–1 km) for all observing nights of 2017 and 2018. See the legends for details.

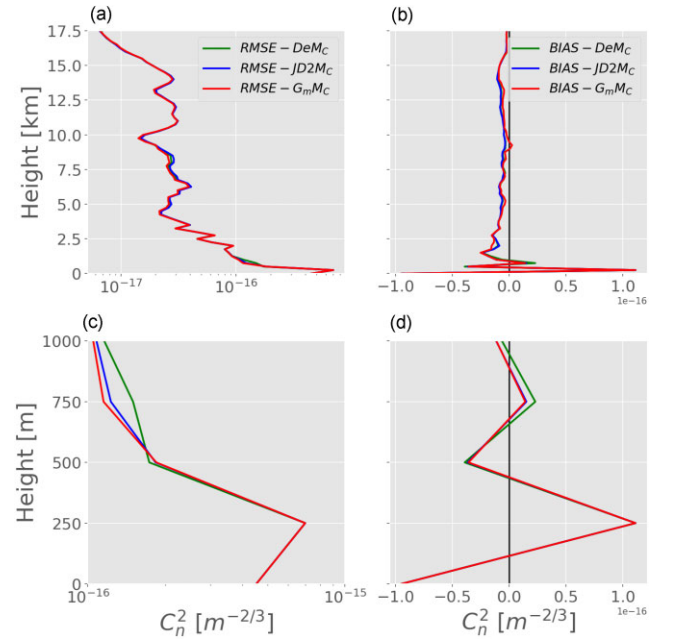


**Figure 8.** The  $C_n^2$  (a) RMSE and (b) BIAS profiles calculated between the three calibrated models and observations for all observing nights of 2017 and 2018. (c) and (d) show a zoom-in to panels (a) and (b), respectively, between the surface and 1 km height.

is still much less than that observed during the nights of 2017 and 2018.

The profiles of mean BIAS and RMSE between calibrated-mixed models and observations show that all calibrated models underestimate observations above the PBL. In contrast, they tend to overestimate them within it (Fig. 8b,d). In addition, all calibrated models show similar results representing the observing conditions, mainly above the PBL, although the  $G_m$ M<sub>C</sub> model shows a slightly better agreement with observations than the other two models (Fig. 8a,c). The largest difference among calibrated models is shown within the PBL (specifically at 250 m height), where  $C_n^2$  errors are an order of magnitude larger than those reported above it (Fig. 8a).

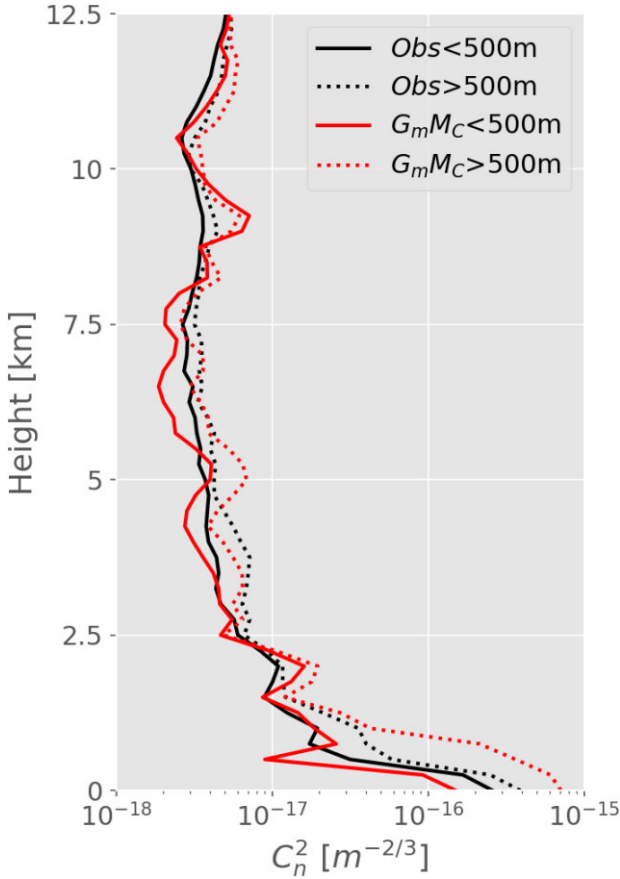


**Figure 9.** Median  $C_n^2$  profiles from the S–SCIDAR and the mixed calibrated model  $G_mM_C$ , for the observing nights of 2017 and 2018. Solid lines represent the times when the PBLH  $\leq 500$  m (67 per cent of the time), whereas the dotted lines represent the times when the PBLH  $> 500$  m (33 per cent of the time). See the legend for details.

### 3.3.1 $C_n^2$ profiles during times with low and high PBLH

As was shown in Section 3.2, using the mean PBLH averaged over all the observing nights (PBLH<sub>all</sub>) to calculate the  $C_n^2$  profile gives less error than using the PBLH every 10 min (PBLH<sub>10m</sub>). However,

we include this short section to show how different is the calculated  $C_n^2$  profile when the model forecasts a PBLH above 500 m to that when the PBLH is below that altitude to better characterize the  $C_n^2$  over the observing site. To this aim, we calculated the  $C_n^2$  profile using the PBLH<sub>10m</sub> and grouped it into two categories: those when the PBLH  $\leq 500$  m (accounting for 67 per cent of cases, see Fig. 4) and those when the PBLH  $> 500$  m (accounting for 33 per cent of cases). In addition, we applied the calibration method described in Section 2.4. Since the three models showed very similar results, we are showing here the results from only one model:  $G_mM_C$ .

The observed  $C_n^2$  when the PBLH  $\leq 500$  m shows lower values in the whole atmospheric column than that when the PBLH  $> 500$  m (Fig. 9). All models underestimate the observed profile at mostly all heights for the cases when the PBLH  $\leq 500$  m. On the contrary, all models overestimate the observed profiles when the PBLH  $> 500$  m (Fig. 9). Another important aspect in the comparison between the models and observations is that the errors in the estimated  $C_n^2$  are smaller in all the models at the times when the PBLH  $\leq 500$  m than when the PBLH  $> 500$  m. Overall, the  $C_n^2$  profile is better represented when the turbulence is concentrated closer to the ground surface than when it is spread over a deeper layer.

### 3.4 Seeing

As mentioned in Section 2.3, seeing forecasts were calculated for each calibrated model (DeM<sub>C</sub>, JD2M<sub>C</sub>, and  $G_mM_C$ ) using the constant PBLH<sub>all</sub>, and they were compared with S–SCIDAR observations, every 10 min. Scatter plots between the simulated seeing from the three calibrated models and observations for all nights of 2017 and 2018 show similar and weak linear correlations (Fig. 10). The three calibrated models mainly underestimate observations, but they show relatively low RMSE values ( $\leq 0.32$  arcsec). The simulated seeing from the  $G_mM_C$  model shows a slightly better agreement with observations, indicated by a bit larger correlation (0.41) and smaller RMSE (0.30 arcsec) than the other models (Fig. 10c). In addition, the best linear fit to the  $G_mM_C$  model falls a bit closer to the 1:1 line than similar fitted lines for the other models.

Fig. 11 shows the frequency distribution of observed and simulated seeing values from the three calibrated models for all observing nights of 2017 and 2018. As previously mentioned, the three calibrated models underestimate the observations. However, the seeing underestimation is slightly less in  $G_mM_C$ , and its seeing

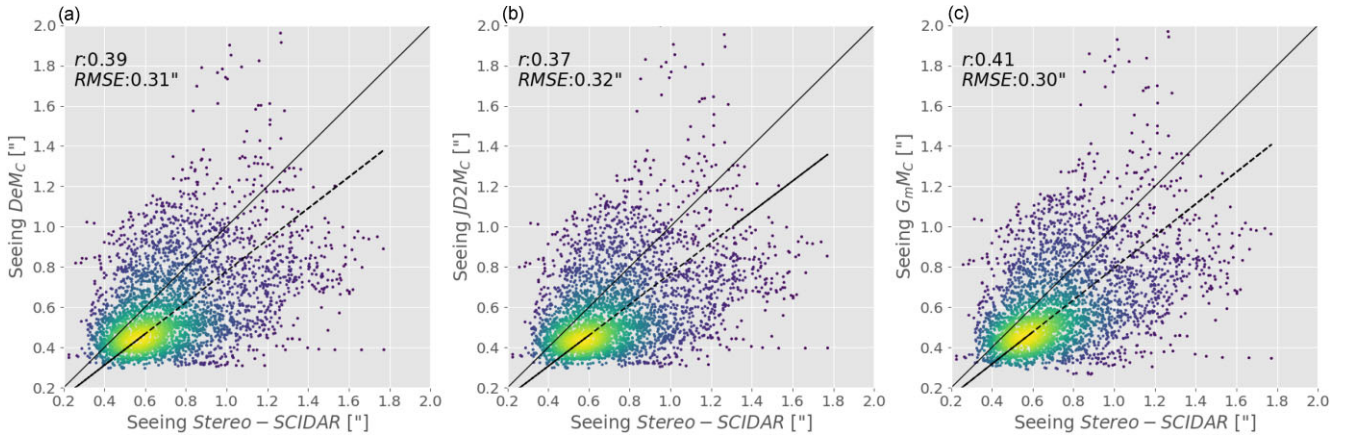


**Figure 10.** Scatter plots between the observed and simulated seeing values from (a) DeM<sub>C</sub>, (b) JD2M<sub>C</sub>, and (c)  $G_mM_C$  calibrated models, calculated for all observing nights of 2017 and 2018. The RMSE and the linear correlation coefficient are indicated on each plot. Solid and dashed lines correspond to the 1:1 line and the best linear fit, respectively.

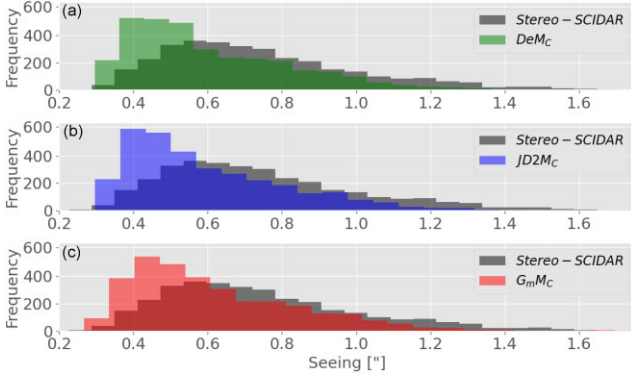


**Figure 11.** Seeing distributions from observations and simulated from (a) DeM<sub>C</sub>, (b) JD2M<sub>C</sub>, and (c) G<sub>m</sub>M<sub>C</sub> calibrated models for all observing nights of 2017 and 2018.

distribution is closer to that observed. In addition, the G<sub>m</sub>M<sub>C</sub> model can better represent the very high seeing values observed in that period, whereas the other two models (DeM<sub>C</sub> and JD2M<sub>C</sub>) shows difficulty representing seeing values larger than 1.2 arcsec.

Table 5 summarizes the RMSE and mean BIAS obtained for the simulated seeing in this and other recent studies conducted at the Paranal observatory to put our results in context. In this study, we obtained a bit lower RMSE (0.30 arcsec) and a similar mean BIAS (−0.1 arcsec) with the calibrated G<sub>m</sub>M<sub>C</sub> model than that obtained in Osborn & Sarazin (2018) with the S–SCIDAR. It is important to note that the estimated seeing reported in both studies underestimates the observed seeing values. Another important aspect to highlight is that the study of Osborn & Sarazin (2018), which uses the same S–SCIDAR data employed in this work, calibrates its model using 50 per cent of the total data, and the period of data used in the calibration process was also included in the comparison. That may be one of the reasons they obtain a very small mean BIAS (−0.01). On the contrary, we only used the nights of 2016 (corresponding to 15 per cent of the data) for the calibration process in this study, and that data was not used in the final comparison. Furthermore, Table 5 also shows the seeing statistics obtained in other studies at Paranal using the Differential Image Motion Monitor (DIMM) installed at that site. The comparison between the simulated seeing obtained with the calibrated G<sub>m</sub>M<sub>C</sub> model and DIMM observations during the observing nights of 2017–2018 shows that we obtained a bit larger RMSE than those obtained in other studies using mesoscale models, whereas our RMSE is a bit lower than those shown in studies using GCM models. On the other hand, we obtained a bit larger BIAS than those reported.

To shed some light on identifying the conditions present during the times with the largest errors in the estimated seeing, we analyse the wind shear, the potential temperature gradient, and the TKE over the 0–500 m layer on each of the three models. Again, since the results from the three models were very similar, we present here only the analysis of the mixed model G<sub>m</sub>M. In addition, we investigate whether the same results are obtained when we apply the calibration

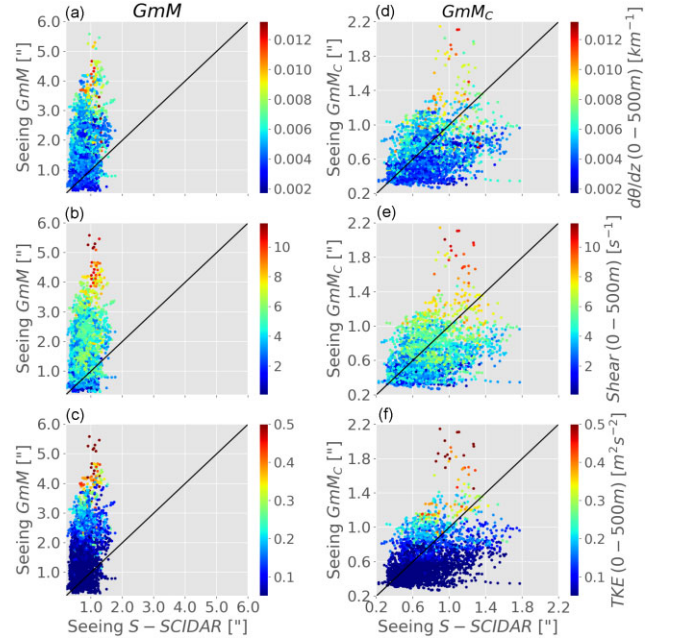


**Figure 12.** Scatter plots between the observed and simulated seeing values from the G<sub>m</sub>M model for all the observing nights of 2016–2018. Circles are colour-coded based on (a) the vertical potential temperature gradient, (b) the wind shear, and (c) the TKE calculated in the 0–500 m layer. (d)–(f) are the same as (a)–(c), but for the mixed-calibrated G<sub>m</sub>M<sub>C</sub> model, calculated for all observing nights of 2017 and 2018.

to the mixed model (G<sub>m</sub>M<sub>C</sub>). Scatter plots between the observed and the estimated seeing from the mixed G<sub>m</sub>M model show that when the atmosphere is more stable, and the vertical wind shear increases in the 0–500 m, the largest TKE values are favoured, which provide the largest seeing errors (Fig 12a–c). The contrary occurs when the 0–500 m layer is less stable, the wind shear is weak and the TKE decreases. When we apply the calibration, the estimated seeing overestimates the observations when the 0–500 m layer is more stable, and the vertical wind shear and TKE show the largest values (Fig 12d–f). As we showed in the previous subsection, this seems to occur for higher PBLs. On the other hand, the estimated seeing underestimates the observations when the 0–500 m layer is less stable, and the vertical wind shear and TKE show the lowest values, which seems to happen for lower PBLs. Similar results are obtained when we analysed the potential temperature gradient, the wind shear, and the TKE over the 0–1000 m layer.

Finally, we present the results of the observed and simulated seeing from the three calibrated models for four continuous nights between 2017 December 13 to 16 (Fig. 13) every 10 min. The three calibrated models represent reasonably well the observed time evolution of seeing, although a slightly better performance is indicated by the G<sub>m</sub>M<sub>C</sub> model, particularly during the highest seeing values (i.e. the night of 2017 December 14).

**Table 5.** Reported seeing statistics in this and other studies on Paranal observatory.

Parameter	Instrument	Ye (2011)		Masciadri et al. (2017)		Osborn & Sarazin (2018)		This study: G <sub>m</sub> M <sub>C</sub>	
		BIAS	RMSE	BIAS	RMSE	BIAS	RMSE	BIAS	RMSE
Seeing	S-SCIDAR	–	–	–	–	−0.01 arcsec	0.31 arcsec	−0.1 arcsec	0.30 arcsec
	DIMM	−0.09 arcsec	0.36 arcsec	−0.09 arcsec	0.48 arcsec	–	–	−0.2 arcsec	0.46 arcsec

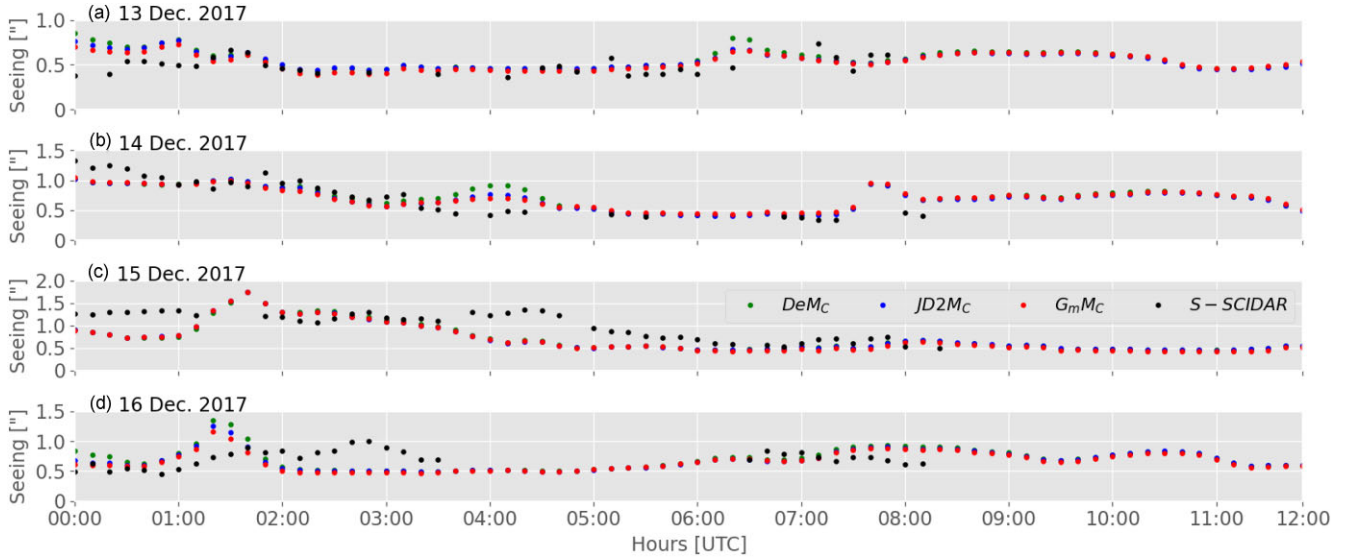


**Figure 13.** Time evolution of observed seeing (black dots) from S–SCIDAR and simulated seeing from DeM<sub>C</sub>, JD2M<sub>C</sub>, and G<sub>m</sub>M<sub>C</sub> models during the nights of 2017 December 13–16.

#### 4 CONCLUSIONS AND DISCUSSION

In this study, we applied a methodology to estimate the vertical distribution of  $C_n^2$  and the seeing values at Paranal Observatory in Chile using a high-resolution numerical simulation from the WRF model for several nights between 2016 and 2018. Our methodology combines the method described in Masciadri & Jabouille (2001) to estimate  $C_n^2$  values within the planetary boundary layer (PBL) with another method to estimate the  $C_n^2$  in the free atmosphere (above the PBL). We tested our methodology using the Dewan (De), a modified one-layer Jackson–Dewan (JD2), and Gladstone ( $G_m$ ) models for the free atmosphere. The  $C_n^2$  model implemented within the PBL uses the turbulent kinetic energy (TKE), which, together with the PBL height, is provided by the PBL parametrization in the WRF model. We used the simulated mean PBL height averaged over all the observing nights to calculate the  $C_n^2$  profile at each simulation time since we found lower errors compared to observations. In addition to the implemented mixed model, we also applied a calibration method using data from 2016 to improve the estimated  $C_n^2$  profiles for all observing nights of 2017 and 2018.

The simulated wind speed and direction from the WRF model were assessed with estimations from the S–SCIDAR for all observing nights between 2016 and 2018. The model represented reasonably well the wind speeds from the surface to 6 km, with RMSE values even lower than  $3 \text{ m s}^{-1}$  at some heights and a correlation coefficient larger than 0.7. The performance of the model largely decreases in the 6–12 km layer, overestimating the observations with RMSE values  $> 6 \text{ m s}^{-1}$ . However, it is important to note that Osborn et al. (2016) showed that the S–SCIDAR underestimated the observed radiosonde wind speeds at La Palma for values  $> 30 \text{ m s}^{-1}$  (their Fig. 11), which are those typically found at higher altitudes. We found similar results in Paranal. The S–SCIDAR underestimates the wind speeds from the Antofagasta radiosonde at higher heights (wind speeds  $> 25 \text{ m s}^{-1}$ ), where the model shows the largest errors. In addition, the model shows a close agreement with the Antofagasta radiosonde over the whole atmospheric column. This adds some uncertainty to the poor performance of the model at higher heights, possibly indicating that the model may be representing the wind speed much better than that indicated in the results. The wind direction, on the other hand,

is better represented by the model at higher heights. However, the statistics found near the surface are in agreement with other studies over complex terrain (Jiménez & Dudhia 2013; Gómez-Navarro, Raible & Dierer 2015). Overall, these results support using the WRF simulation to estimate the  $C_n^2$  profiles over the Paranal observatory.

The combined models (DeM, JD2M, and  $G_m$ M) represent better the observed  $C_n^2$  profiles than the original Dewan (De), Jackson–Dewan (JD2), and Gladstone ( $G_m$ ) models, mainly within the PBL. However, it is important to note that Dewan (De) and Jackson–Dewan (JD2) methods do not include the PBL in their original formulation. Despite this improvement, still, large differences between the combined models and observations persist in the free atmosphere. The application of a calibration method to the mixed models (DeM<sub>C</sub>, JD2M<sub>C</sub>, and  $G_m$ M<sub>C</sub>) improves the  $C_n^2$  profile in the whole atmospheric column, even within the PBL, underestimating, in general, the observations, except at specific heights within the PBL. None the less, the most important result is that all calibrated models show very similar results, independent of the  $C_n^2$  model used, which highlights its importance in improving the  $C_n^2$  and seeing forecasts over the region.

Seeing forecasts from calibrated models (DeM<sub>C</sub>, JD2M<sub>C</sub>, and  $G_m$ M<sub>C</sub>) show similar results with observations, although the  $G_m$ M<sub>C</sub> model shows a slightly better performance. Statistical metrics obtained from this study are similar and, in some cases, slightly better compared with previous studies in Paranal using mesoscale and global circulation models (Table 5). Therefore, due to its performance and rapid execution, our methodology may be a very good alternative to provide operational forecasts of  $C_n^2$  profiles and the seeing at Paranal and could also be implemented at other astronomical sites.

The De, JD, and  $G_m$ M models were derived from geographical and atmospheric conditions that may be different from those at Paranal. The combination of models shows an improvement in the PBL, better representing the observed  $C_n^2$ . The method applied within the PBL uses TKE values from the PBL parametrization in the WRF model. Since other PBL parametrizations that explicitly solve the TKE are available in the model, this opens an opportunity to explore other PBL schemes that may improve the  $C_n^2$  forecasts within the PBL and the subsequent seeing estimation. In addition, other methods to

calculate the  $C_n^2$  profile and the seeing are available in the literature that can be implemented using high-resolution WRF simulations to test whether they may provide better forecasts. These are topics of research that are currently underway.

The current study showed that the most stable conditions at Paranal are accompanied by the largest wind shear values within the PBL, generating more turbulent nights. These conditions are associated with the lowest model performance estimating the optical turbulence at the site. The simulation employed in this study used a terrain with a 1 km horizontal resolution, which still is coarse to accurately represent the complex terrain of the region. Conducting a simulation with an improved and higher resolution model terrain may result in a better representation of the boundary layer at Paranal, consequently giving a more accurate estimation of the optical turbulence. In addition, new model versions include more complex parametrizations and parameters that may better simulate the atmospheric conditions over complex terrain. Testing those new model features may improve our results.

## ACKNOWLEDGEMENTS

We acknowledge the reviewer for the positive comments that helped improve the quality of the manuscript. Authors OC, JCM, and CM acknowledge support from Centro de Estudios Atmosféricos y Cambio Climático (CEACC), Universidad de Valparaíso, Chile.

## DATA AVAILABILITY

Due to the large disc space occupied by the outputs from the WRF simulation generated for this study, they are not stored on any public data request system. However, fields from this simulation can be made available to any interested researcher upon request. Data from the Antofagasta radiosonde can be downloaded at <https://weather.uwyo.edu/upperair/sounding.html>.

## REFERENCES

- Banks R. F., Tiana-Alsina J., Baldasano J. M., Rocadenbosch F., Papayannis A., Solomos S., Tzani C. G., 2016, *Atmos. Res.*, 176, 185
- Basu S., 2015, *Opt. Lett.*, 40, 4130
- Bauer P., Thorpe A., Brunet G., 2015, *Nature*, 525, 47
- Businger S., Cherubini T., 2011, Seeing Clearly: The Impact of Atmospheric Turbulence on the Propagation of Extraterrestrial Radiation. Virtualbookworm.com Publishing, Incorporated, Texas
- Chacón A. et al., 2010, in Stepp L. M., Gilmozzi R., Hall H. J., eds, Proc. SPIE Conf. Ser. Vol. 7733, in Ground-based and Airborne Telescopes III. SPIE, Bellingham, p. 77334K
- Cherubini T., Businger S., 2013, *Am. Meteorol. Soc.*, 52, 498
- Cherubini T., Businger S., Lyman R., 2008, *J. Appl. Meteorol. Climatol.*, 47, 1140
- Coulman C., Vernin J., Coqueugnot Y., Caccia J., 1988, *Appl. Opt.*, 27, 155
- Cuevas O., Curé M., Escárate P., 2018, in Marshall H. K., Spyromilio J., eds, Proc. SPIE Conf. Ser. Vol. 10700, Ground-based and Airborne Telescopes VII. SPIE, Bellingham, p. 1547
- Dewan E. M., Good R. E., Beland B., Brown J., 1993, A Model for  $C_n^2$  (optical turbulence) Profiles using Radiosonde Data. No. 1121 in Environmental Research Papers, Directorate of Geophysics, Air Force Materiel Command, MA, USA

- Fiorino S. T., 2014, Imaging and Applied Optics 2014. Optica Publishing Group, OSA Technical Digest(online) [opg.optica.org/abstract.cfm?URI=pcDVT-2014-PMIE.1](http://opg.optica.org/abstract.cfm?URI=pcDVT-2014-PMIE.1)
- Giordano C., Vernin J., Vázquez Ramió H., Muñoz-Tunón C., Varela A. M., Trinquet H., 2013, *MNRAS*, 430, 3102
- Giordano C., Vernin J., Trinquet H., Muñoz-Tunón C., 2014, *MNRAS*, 440, 1964
- Gómez-Navarro J. J., Raible C. C., Dierer S., 2015, *Geosci. Model Dev.*, 8, 3349
- Grell G. A., Dévényi D., 2002, *Geophys. Res. Lett.*, 29, 38
- Hong S.-Y., Dudhia J., Chen S.-H., 2004, *Mon. Weather Rev.*, 132, 103
- Iacono M. J., Delamere J. S., Mlawer E. J., Shephard M. W., Clough S. A., Collins W. D., 2008, *J. Geophys. Res. Atmos.*, 113, D13103
- Jackson A., 2004, Modified-Dewan Optical Turbulence Parameterizations. Air Force Research Lab, Space Vehicles Directorate, Air Force Materiel Command, Hanscom AFB, MA, USA
- Jiménez P. A., Dudhia J., 2013, *J. Appl. Meteorol. Climatol.*, 52, 1610
- Lyman R., Cherubini T., Businger S., 2020, *MNRAS*, 496, 4734
- Masciadri E., Jabouille P., 2001, *A&A*, 376, 727
- Masciadri E., Vernin J., Bougeault P., 1999, *Astron. Astrophys. Suppl. Ser.*, 137, 185
- Masciadri E., Lascaux F., Turchi A., Fini L., 2017, *MNRAS*, 466, 520
- Masciadri E., Turchi A., Fini L., 2023, *MNRAS*, 523, 3487
- National Centers for Environmental Prediction, National Weather Service, NOAA, U.S. Department of Commerce, 2015, NCEP GDAS/FNL 0.25 Degree Global Tropospheric Analyses and Forecast Grids, available at: <https://rda.ucar.edu/datasets/ds083.3/>
- Niu G.-Y. et al., 2011, *J. Geophys. Res. Atmos.*, 116, D12109
- Osborn J., Sarazin M., 2018, *MNRAS*, 480, 1278
- Osborn J., Butterley T., Townson M., Reeves A., Morris T., Wilson R., 2016, *MNRAS*, 464, 3998
- Osborn J. et al., 2018, *MNRAS*, 478, 825
- Quatresooz F., Griffiths R., Bardou L., Wilson R., Osborn J., Vanhoenacker-Janvier D., Oestges C., 2023, *Opt. Express*, 31, 33850
- Roddier F., 1981, *Prog. Opt.*, 19, 281
- Roşu I.-A., Ferrarese S., Radinschi I., Ciocan V., Cazacu M.-M., 2019, *Atmosphere*, 10, 559
- Salfate I., Marin J. C., Cuevas O., Montecinos S., 2020, *Wind Energy*, 23, 1939
- Shepherd H. W., Osborn J., Wilson R. W., Butterley T., Avila R., Dhillon V. S., Morris T. J., 2013, *MNRAS*, 437, 3568
- Shikhovtsev A. Y. et al., 2023, *Appl. Sci.*, 13, 1282
- Skamarock W. C. et al., 2008, A description of the Advanced Research WRF Version 3 (No. NCAR/TN-475+STR). University Corporation for Atmospheric Research, National Center for Atmospheric Research, Boulder, Colorado, USA
- Stull R., 1988, An Introduction to Boundary Layer Meteorology. Atmospheric and Oceanographic Sciences Library, Springer-Verlag, Berlin
- Sukoriansky S., Galperin B., Perov V., 2005, *Boundary-Layer Meteorol.*, 117, 231
- Tatarski'i V., 1961, Wave Propagation in a Turbulent Medium. McGraw-Hill, University of California, New York
- Trinquet H., Vernin J., 2007, *Environ. Fluid Mech.*, 7, 397
- Vernin J., Azouit M., 1983, *J. Opt.*, 14, 131
- Vernin J., Muñoz-Tunón C., 1992, *A&A*, 257, 811
- Xie B., Fung J. C. H., Chan A., Lau A., 2012, *J. Geophys. Res. Atmos.*, 117, D12103
- Yang Q., Wu X., Wang Z., Hu X., Guo Y., Qing C., 2022, *MNRAS*, 515, 1788
- Ye Q.-Z., 2011, *PASP*, 123, 113

This paper has been typeset from a  $\text{\TeX}/\text{\LaTeX}$  file prepared by the author.